INTERNATIONAL JOURNAL OF PRECISION ENGINEERING AND MANUFACTURING Vol. 19, No. 7, pp. 1019-1026 JULY 2018 / 1019

REGULAR PAPER

DOI: 10.1007/s12541-018-0120-1
ISSN 2234-7593 (Print) / 2005-4602 (Online)

Static and Dynamic Analyses of a 6-DOF Ultra-Precision Parallel Mechanism

Hyun-Pyo Shin[1,#] and **Jun-Hee Moon**[2]

1 School of Robot and Automation Engineering, Dongyang Mirae University, 445, Gyeongin-ro, Guro-gu, Seoul, 08221, Republic of Korea
2 Department of Mechatronics Engineering, Yuhan University, 590, Gyeongin-ro, Bucheon-si, Gyeonggi-do, 14780, Republic of Korea
Corresponding Author / E-mail: hpshin@dongyang.ac.kr, TEL: +82-2-2610-1816
ORCID: 0000-0002-1779-0577

KEYWORDS: Flexure hinge, Parallel mechanism, Lost motion, Modal analysis, Linear mapping matrix

Flexure-based ultra-precision parallel mechanisms have inherent difference between input and actual output. Lost motion that stems from elasticity of flexure hinges in the parallel mechanism results in gain reduction of actuation. Therefore, static analysis is carried out by calculating directional stiffness and lost motions of actuation units, and is verified by finite element analysis (FEA). Dynamic analysis is performed based on modal analysis with linear mapping matrices to identify the dynamics of the parallel mechanism. Theoretical modal analysis is carried out and then verified by FEA and experiment. The identified lost motion and dynamics are expected to be exploited respectively for gain adjustment and dynamics enhancement for future studies on flexure-based precision parallel mechanisms with 6-DOF.

Manuscript received: August 16, 2017 / Revised: January 9, 2018 / Accepted: January 19, 2018

1. Introduction

Micro-positioning has become an essential issue in many fields, such as biological cell manipulation, microsurgery operation, fiber optic alignment, wafer alignment, and micromachining.[1] Among these applications, a main task is to manipulate micro-scale objects with micro/nanometer precision. For these applications, high precision, large motion range, multi-axis motion, high positioning stability, and compact size are needed.[2,3] Especially, wafer alignment and bonding processes require both high precision and large force generation, which are difficult to obtain simultaneously.

Conventional positioning stages based on servomotors, ball screws, and rigid linkages have limited applicability in micro/nano-technology areas due to their inherent problems of clearance, friction, and backlash. In contrast, compliant mechanisms in which elastic deformation is used to transfer motion are suitable for ultra-precision applications because they offer good repeatability with no wear, friction, and backlash.[4] Moreover, it is well known that parallel mechanisms offer benefits over serial mechanisms in terms of high stiffness, low inertia, large payload capacity, and high precision, whereas serial manipulators typically have larger workspaces and need simple control system. Due to these advantages, many precision positioning stages have adopted parallel mechanisms.[5,6]

Various structures and actuators are applied to the precision positioning stages. Gao and Swei[7] combined the in-plane (x, y-translations, z-rotation) and out-of-plane (x, y-rotations, z-translation) motions in a serial mechanism. The wafer stage of a 6-DOF (degrees-of-freedom) compliant mechanism for single-step nano-imprint lithography, consisting of an inner mechanism and outer mechanism, is presented.[8] A piezoelectrically actuated 6-DOF stage for micro-positioning is developed by using orthogonal actuators and a lever linkage.[9]

With regard to characterization of flexure-based positioning stages, the effective stiffness, mass, and resonance frequency in the vertical direction of a monolithic XY nanopositioning stage was derived by theoretical analysis and the results were compared to FEA.[10] A finite element analysis-based response surface methodology was utilized to solve the multi-objective optimization problems and thus the static and dynamic characteristics of the positioning platform were improved.[11]

Control is critical concern for the design of precision mechanisms. Hu et al.[12] designed a 6-DOF hybrid series-parallel mechanism based on PZT actuator and applied real-time feedback to reduce the effects of calibration error, nonlinearity, thermal drift of structure, and sensor drift. Choi et al.[13] performed optimal design of the displacement amplification mechanism and implemented precision motion by designing Preisach model feed-forward and PID feedback controllers. Yue et al.[14] proposed

a new approach investigating the relationship among input-force, payload, stiffness, and displacement (IPSD) of the 3-DOF perpendicular parallel micro-manipulator to achieve highly accurate control. Kim et al.[5] presented an active vibration control system which is constructed based on a novel three-DOF precision micro-stage.

Theoretical modellings and their application to early stage design were discussed in several previous works. Awtar and Sen[15] presented a highly generalized and accurate closed-form parametric load-displacement model for two-dimensional beam flexures. A symbolic formulation for analytical compliance analysis and synthesis of flexure mechanisms was developed based on the screw theory that characterizes flexure deformations with motion twists and loadings with force wrenches.[16] Lu and Peng[17] derived an accurate model of the multi-leaf spring based nano-stage by incorporating the effect of cross axis input force.

This paper describes static and dynamic analyses for a novel 6-DOF ultra-precision parallel mechanism that utilize flexure hinges and PZT actuators. The precision mechanism was designed for wafer level lens bonding.[18] Our previous research has recognized the need to clearly identify the issues related to precise control. So it is the purpose of this study to analyze and characterize the issues. The followings are detailed purposes.

First, it is necessary to identify lost motions as an obstacle to accurate positioning. Flexure-based parallel mechanism with PZT actuators are under two major detrimental effects against precise positioning: piezoelectric material effect and elasticity-inducing effect. Since the piezoelectric material effect including hysteresis and creep has been extensively studied, we just focus on the identification of the elasticity-inducing effect, which produces so-called 'lost motion', which results in inaccurate positioning.

Second, it is essential to identify dynamics of the 6-DOF ultra-precision parallel mechanism to check control bandwidth. For this, theoretical modal analysis is attempted to find the possibility to identify the influences of design variable, which can be useful when specification alteration. The results are compared with FEA and experiment for verification.

This paper is organized as follows. In Section 2, design issues and structural features of the precision parallel mechanism are explained. Static analyses on the horizontal and vertical actuation units are performed in Section 3. Dynamic analysis and related experimental results are presented in Section 4. Finally, some concluding remarks are provided in Section 5.

2. Structure of 6-DOF Ultra-Precision Parallel Mechanism

2.1 Double triangular configuration of actuators

The 6-DOF ultra-precision mechanism is shown in Fig. 1. This 6-DOF precision mechanism is designed to minimize overall size, to share payload equally transmitted to each actuation unit, and to maximize tilt motion ranges (x-, y-rotations). For these features, the horizontal and vertical actuation units which take charge of in-plane and out-of-plane motions respectively are configured to have double triangular structure. By configuring the horizontal actuation units as inner triangle and the vertical actuation units as outer triangle, z-

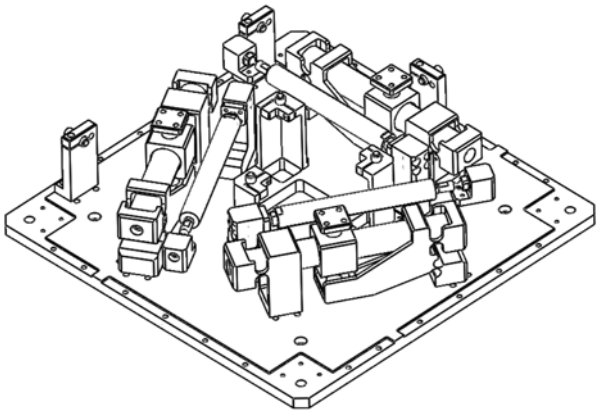

Fig. 1 6-DOF ultra-precision parallel mechanism (upper parts are removed for understanding)

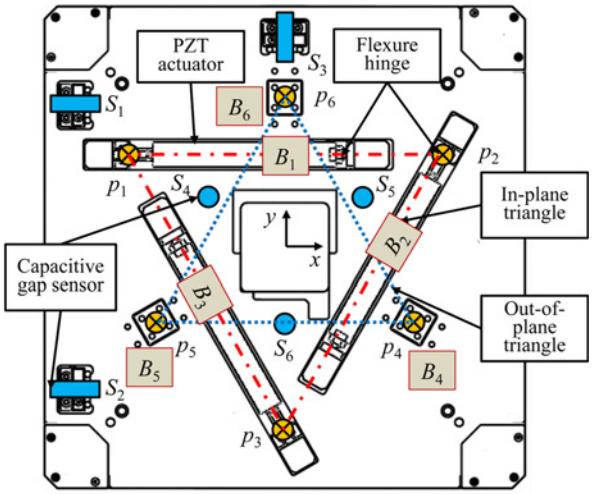

S_i: Sensor, B_i: Actuator
p_i: Position of hinge directly attached to end-effector (upper plate)

Fig. 2 Double triangular structure and positions of sensors and actuators

rotation range and x-, y-rotation sensitivities are maximized while stably supporting vertical payload such as wafer bonding pressure. Moreover, the double triangular structure can be applied to equip optical projection modules through the center square hole.

To implement precision motions, PZT actuators (B_1, B_2, B_3: PSt 1000/10/150 VS18 - maximum stroke of 150 μm, maximum load of 5000 N, resonance frequency of 5 kHz, and stiffness of 17 N/μm / B_4, B_5, B_6: PSt 1000/16/200 VS25 - maximum stroke of 200 μm, maximum load of 15000 N, resonance frequency of 4 kHz, and stiffness of 35 N/μm, Piezomechnik) which have high resolution and fast response with no backlash are applied. Capacitive gap sensors (C36 - sensing range of 500 μm and resolution of 10 nm, Lion Precision) with sensing resolution of nano level are used. Six actuation units and capacitive gap sensors are positioned as in Fig. 2. The three sensors are positioned to parallel to the bottom plate of precision mechanism for sensing the in-plane motion while the other sensors are positioned to perpendicular to the bottom plate for sensing the out-of-plane motion. All the surfaces of opposite parts to the sensors are processed to have fine surface

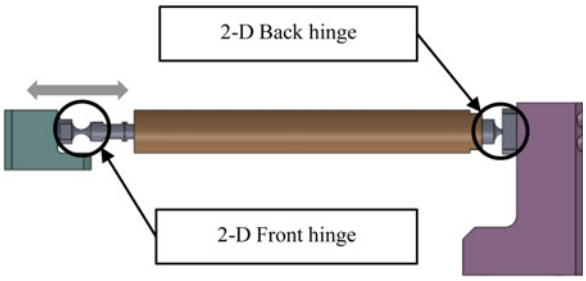

Fig. 3 Horizontal actuation unit

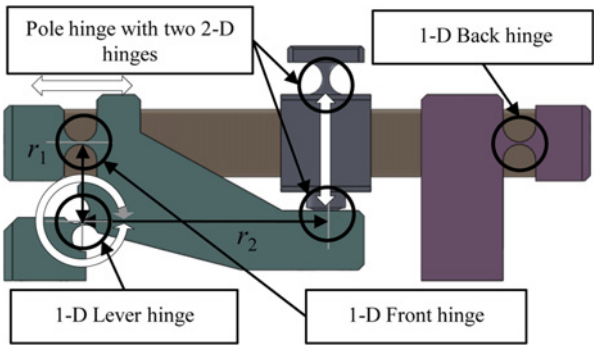

Fig. 4 Vertical actuation unit

roughness. By sensing the motion of precision mechanism with six capacitive gap sensors, closed-loop control is realized. Material used for all hinges are stainless steel SUS420 (yield stress: 1360 MN/m^2). Size of the precision mechanism is 380 mm × 380 mm × 115 mm (W × L × H). In addition, the *x*-, *y*-translational strokes of the precision stage is ±50 μm and the *z*-translational stroke is ±150 μm, the *x*-, *y*-rotational strokes is ±733 μrad (±0.042°) and the *z*-rotational stroke is ±244 μrad (±0.014°).

2.2 Structure of actuation units

Horizontal and vertical actuation units are shown in Figs. 3 and 4 respectively. Arrows mean motion directions. The horizontal actuation unit is composed of one PZT actuator and two 2-D flexure hinges (2-D hinge moves along 2-dimensional motion axes) attached front and back of the actuator as in Fig. 3. Through this configuration of hinges, the horizontal actuation unit can realize high motion DOF. Moreover, the actuator can be protected from sudden external impact. Thickness of the 2-D front and back hinges are 1.54 mm.

The vertical actuation unit shown in Fig. 4 is composed of one PZT actuator, two 1-D flexure hinges (1-D hinge moves along 1-dimensional motion axis) attached front and back of the actuator, one pole hinge with two 2-D flexure hinges which one side is connected to the end-effector, and one 1-D flexure lever hinge which changes the motion direction by 90 degrees. Especially, the vertical actuation unit has novel overlapping structure. To minimize occupation space and to lower the height of the precision mechanism for high stiffness, each hinge block is designed to envelop the entire actuator. In addition, a through hole is processed in the middle of pole hinge block for actuator placement. By virtue of applying lever mechanism, *z*-translation and *x*-, *y*-rotations are amplified by the amount of amplification ratio (= r_2/r_1).

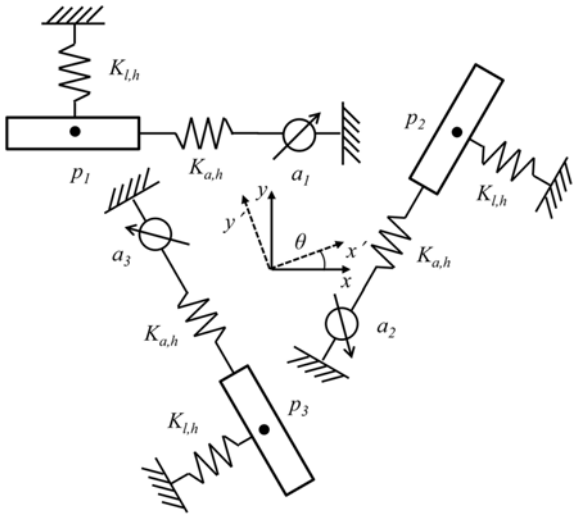

Fig. 5 Schematic diagram of the horizontal actuation units in the triangular configuration

In this study, the amplification ratio is set as three. All the hinges are aligned in horizontal and vertical directions to minimize parasitic motions. The vertical actuation unit has original structure optimized to implement precision performance, long translation range with minimum size. Thickness of the 1-D front and back hinges are 0.85 mm, 1-D lever hinge is 1 mm, and two 2-D hinge of the pole hinge block are 2.37 mm respectively.

3. Static Analysis of 6-DOF Ultra-Precision Parallel Mechanism

3.1 Horizontal stiffness non-directionality by the triangular configuration of horizontal actuation units

To make the parallel mechanism have non-directional horizontal stiffness, we devised the triangular configuration of the horizontal actuation units as shown in Fig. 5. The non-directionality can be justified by the following theoretical derivation. In Fig. 5, each horizontal actuation unit have the same axial stiffness $K_{a,h}$ and lateral stiffness $K_{l,h}$. If a force F is applied to the moving part of the parallel mechanism at an angle of θ from *x*-axis (*x*′-axis in Fig. 5), a deformation d is generated in the same direction. Since the three horizontal actuation units are placed with angular spacing of 120 degrees, the applied force F can be expressed as Eq. (1).

$$\begin{aligned} F = K_{eq,h}\delta = K_{l,h}\delta(\sin^2\theta + \sin^2(\theta+120^\circ) + \sin^2(\theta-120^\circ)) \\ + K_{a,h}\delta(\cos^2\theta + \cos^2(\theta+120^\circ) + \cos^2(\theta-120^\circ)) \end{aligned} \quad (1)$$

According to basic rules for trigonometric functions, the equivalent horizontal stiffness $K_{eq,h}$ is obtained from Eq. (1) as follows.

$$K_{eq,h} = 1.5K_{a,h} + 1.5K_{l,h} \quad (2)$$

Eq. (2) shows that the equivalent horizontal stiffness $K_{eq,h}$ has no directionality since the terms with the angle θ are all vanished. The horizontal stiffness of Table 1 calculated by FEA (refer to Fig. 6)

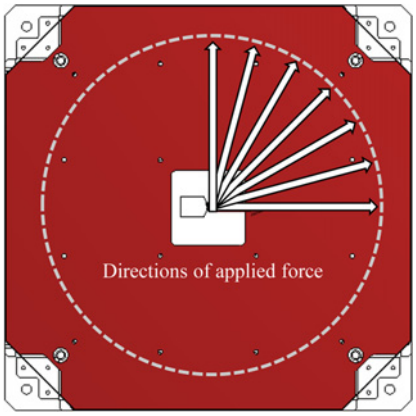

Fig. 6 Applied forces and their directions for stiffness analysis in FEA software (red colored part is moving part which is end-effector)

Table 1 Horizontal stiffness of the moving part according to the angle from *x*-axis (reflecting symmetry, stiffness data from 0 to 90 degrees is listed)

Angle from *x*-axis (degree)	Displacement (μm)	Stiffness (N/μm)
0	41.9	2.39
15	44.0	2.27
30	45.2	2.21
45	45.5	2.20
60	45.0	2.22
75	43.9	2.28
90	41.7	2.40

proves that the strategic triangular configuration of the horizontal actuation units is successful in achieving even horizontal stiffness in every in-plane direction. The force (F) applied here is 100 N. $K_{a,h}$ and $K_{l,h}$ are 10.30 N/μm and 0.0012 N/μm, respectively, which were obtain from FEA for the individual horizontal actuation unit.

3.2 Lost motion of vertical actuation units

Lost motion is considered to be generated when the displacement of actuator is not delivered completely to the end-effector because of the elasticity of flexure hinge. Consequently, it is required to compute amount of lost motion to compensate the motion or to decide appropriate control method for precision positioning.

To compute the lost motion of the vertical actuation unit, we simplified the vertical actuation unit of Fig. 4 to the one of Fig. 7 where the hinges and actuator are substituted to the springs and displacement. When the actuator generates displacement u, the lever hinge rotates by θ and the pole hinge block which corresponds to end-effector moves along vertical direction as much as amplified displacement. ($3r_1$=r_2) Applying the moment equilibrium condition at the center of the lever hinge, Eq. (3) is derived.

$$\sum M = 0 : K_{\theta,2}\theta - r_1 K_1 (u - r_1\theta) + r_2 K_3 (r_2\theta - z) = 0 \tag{3}$$

$$(K_{\theta,2} + r_1^2 K_1 + r_2^2 K_3)\theta = r_1 K_1 u + r_2 K_3 z \tag{4}$$

$$where,\ K_1 = \left(\frac{1}{K_{PZT}} + \frac{2}{K_{a,1}} \right)^{-1} \tag{5}$$

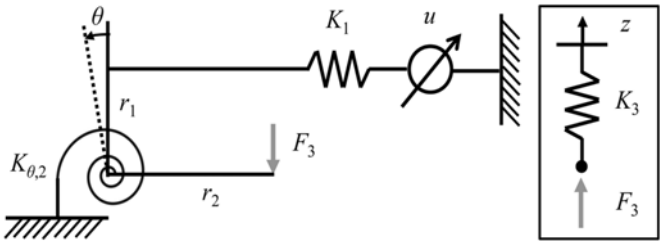

Fig. 7 Schematic diagram of vertical actuation unit for displacement input

In Eq. (4), K_1 is a stiffness including the stiffness of PZT actuator (K_{PZT}) and stiffness of front and back hinges ($K_{a,1}$). $K_{\theta,2}$ and K_3 are stiffness of lever hinge and pole hinge block respectively. r_1 is distance between the centers of front and lever hinges. r_2 is distance between the centers of lever hinge and lower pole hinge of pole hinge block. z is vertical displacement of the pole hinge block. By rearranging Eq. (4) with respect to θ we get Eq. (6).

$$\theta = \frac{r_1 K_1}{K_{\theta,2}\theta + r_1^2 K_1 + r_2^2 K_3} u + \frac{r_2 K_3}{K_{\theta,2}\theta + r_1^2 K_1 + r_2^2 K_3} z \tag{6}$$

The z and K_3 are replaced with F_3 in Fig. 7 to display θ with respect to force. The relationship between F_3 and K_3 is expressed as Eq. (7) and it is transformed into Eq. (8) with respect to θ.

$$F_3 = K_3 (r_2\theta - z) \tag{7}$$

$$\theta = \frac{F_3}{r_2 K_3} + \frac{z}{r_2} \tag{8}$$

As a result, Eq. (3) is simplified to Eq. (9).

$$K_{\theta,2}\theta - r_1 K_1 (u - r_1\theta) + r_2 F_3 = 0 \tag{9}$$

By rearranging Eq. (9) with respect to θ we get Eq. (10).

$$(K_{\theta,2} + r_1^2 K_1)\theta = r_1 K_1 u - r_2 F_3 \tag{10}$$

Therefore, the displacement of end-effector generated by the displacement of PZT actuator u is shown in Eqs. (11) and (12).

$$with\ lost\ motion : z = \frac{r_2/r_1}{1 + \frac{K_{\theta,2}}{r_1^2 K_1}} u - \left(\frac{r_2^2}{K_{\theta,2} + r_1^2 K_1} + \frac{1}{K_3} \right) F_3 \tag{11}$$

$$without\ lost\ motion : z = \frac{r_2}{r_1} u \tag{12}$$

In Eq. (11), the denominator of the first term of right side indicates that lost motion is generated by the stiffness of flexure hinges. The second term shows that dead deflection is consistently generated by the self-load of the end-effector.

Result of lost motion analysis obtained from FEA is shown in Fig. 8. Moreover, the amount of lost motion obtained from theoretical analysis and FEA is listed in Table 2. It is found that they closely coincide with each other by 1% error. In FEA result, difference between the

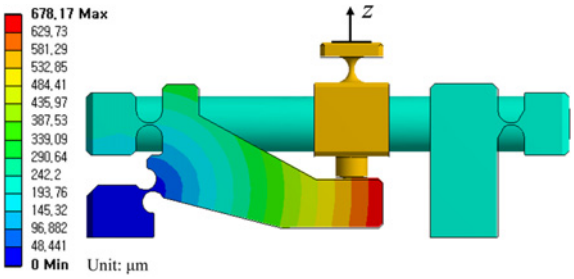

Fig. 8 Amount of lost motion occurred in vertical actuation unit

Table 2 Comparison between theoretical and finite element analysis evaluations for vertical actuation unit

Command (μm)	Theoretical (μm)	FEA (μm)
0	0	0
120	117	116.3
240	234	232.5
360	351	348.8
480	468	465.0
600	585	581.3

commanded and resulting displacements is about 3%. The analysis results show that lost motion is linearly proportional to commanded displacement. The one of objectives of this study is to find out and compensate the lost motion. In the case of this precision mechanism, the amount of lost motion is relatively small and it can be sufficiently compensated by close-loop control. However, it is noticed from this study that lost motion analysis is the necessary procedure in order to design controller prior to the decision of appropriate control strategy, especially, when the system is susceptible to generating large lost motion.

4. Dynamic Analysis of 6-DOF Ultra-Precision Parallel Mechanism

4.1 Linear mapping matrices for coordinate transformation

Dynamic modes or vibration modes reveal the dynamic characteristic of a system. The modal analysis of the flexure-based parallel mechanism started from linear mapping matrices, which is derived from forward and backward kinematics of the mechanism.

The linear mapping matrices, $\mathbf{R}_a$ and $\mathbf{R}_s$, transform coordinates in the control loop for the developed parallel mechanism, as shown in Fig. 9. When a reference command $\mathbf{x}^*$ is given, $\mathbf{R}_a$ produces actuator displacements $\mathbf{a}$. The inverse of $\mathbf{R}_s$ computes the real movement of the precision parallel mechanism $\mathbf{x}$ from the sensor signal $\mathbf{s}$. Eqs. (13) and (14) represent the sensitivity of the i -th output variable to the j -th input variable.

$$\mathbf{R}_a = \left[\frac{\partial a_i}{\partial x_j}\right] \in \Re^{6\times 6} \tag{13}$$

$$\mathbf{R}_s = \left[\frac{\partial s_i}{\partial x_j}\right] \in \Re^{6\times 6} \tag{14}$$

The derivation of Eqs. (13) and (14) can be found in our previous research.[18]

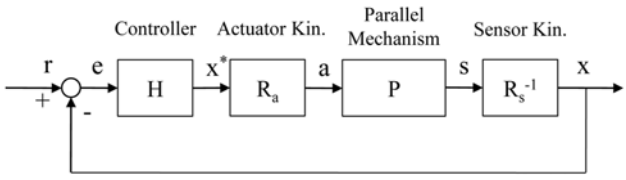

Fig. 9 Control Loop of 6-DOF ultra-precision parallel mechanism

4.2 Theoretical modal analysis

In this Section, we introduce modal analysis by applying the Euler-Lagrange equation and linear mapping matrices. Moreover, FEA result and experimental verification for the analysis are shown.

In a multiple degrees-of-freedom system, Euler-Lagrange's equations can be used to establish the dynamic model and to calculate the natural frequencies of vibration. The non-conservative forces such as friction force can be neglected in flexure-based parallel mechanism. As a result, the Euler-Lagrange equation is given as Eq. (15),

$$\frac{d}{dt}\left(\frac{\partial L}{\partial \dot{q}_i}\right) - \frac{\partial L}{\partial q_i} = 0, \quad i = 1, 2, \ldots, n \tag{15}$$

$$where\ L = T - V \tag{16}$$

In Eqs. (15) and (16), T represents the total kinetic energy of the systems, V denotes the potential energy which includes both strain energy and the potential of any conservative external forces, q_i represent linearly independent generalized coordinates, and n is the number of generalized coordinates, which is also equal to the degree-of-freedom of a system.

Kinetic energy T is represented with respect to the six kinds of motions in the space which is shown as (17),

$$T = \frac{1}{2}m\dot{x}^2 + \frac{1}{2}m\dot{y}^2 + \frac{1}{2}m\dot{z}^2 + \frac{1}{2}I_{xx}\dot{\theta}_x^2 + \frac{1}{2}I_{yy}\dot{\theta}_y^2 + \frac{1}{2}I_{zz}\dot{\theta}_z^2 \tag{17}$$

where m is mass and I is moment of inertia of the end-effector.

Potential energy V is composed of the strain energy induced by displacements of six actuators which is shown as (18),

$$V = \frac{1}{2}K_h(a_1^2 + a_2^2 + a_3^2) + \frac{1}{2}K_v(a_4^2 + a_5^2 + a_6^2) \tag{18}$$

where K_h and K_v represent the stiffness of the horizontal and vertical actuation units respectively. The analysis model presented in this study is based on the assumption that every body of the 6-DOF ultra-precision parallel mechanism is rotating around an axis at a time and contemporarily its inertia matrix is purely diagonal. Therefore, only the axial stiffness is considered. a_i is the displacement of ith actuator. By chain rule, partial derivative of the L with respect to the q_i is represented as,

$$\frac{\partial L}{\partial q_i} = \sum_j \frac{\partial L}{\partial r_j}\frac{\partial r_j}{\partial q_i} \tag{19}$$

Partial derivative of V with respect to x_i is,

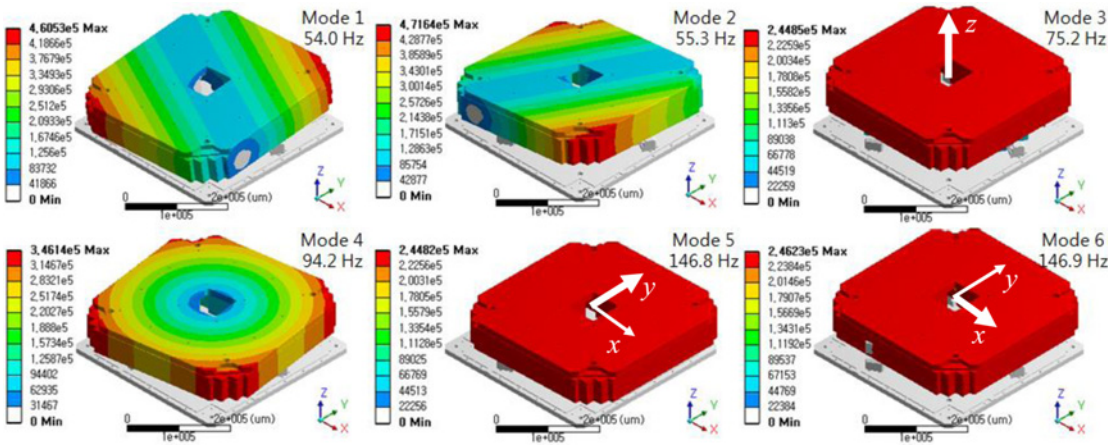

Fig. 10 Modal FEA results for the first six modes

$$\frac{\partial V}{\partial x_i} = K_h\left(a_1\frac{\partial a_1}{\partial x_i} + a_2\frac{\partial a_2}{\partial x_i} + a_3\frac{\partial a_3}{\partial x_i}\right) + K_v\left(a_4\frac{\partial a_4}{\partial x_i} + a_5\frac{\partial a_5}{\partial x_i} + a_6\frac{\partial a_6}{\partial x_i}\right) \tag{20}$$

where, x=[x, y, z, θ_x, θ_y, θ_z].

Eq. (20) is expressed in another form as Eq. (21)

$$\frac{\partial V}{\partial x_i} = K_h\sum_{k=1}^{3}\left(\frac{\partial a_k}{\partial x_i}a_k\right) + K_v\sum_{k=4}^{6}\left(\frac{\partial a_k}{\partial x_i}a_k\right) \tag{21}$$

By substituting Eq. (21) into Eq. (15), we get the following relationship.

$$-\frac{\partial L}{\partial x_i} = \frac{\partial V}{\partial x_i} = K_h\sum_{h=1}^{3}\left[\mathbf{R}_a(h,i)\sum_{j=1}^{6}\mathbf{R}_a(h,j)x_j\right] + K_v\sum_{h=4}^{6}\left[\mathbf{R}_a(h,i)\sum_{j=1}^{6}\mathbf{R}_a(h,j)x_j\right] \tag{22}$$

Accordingly, the Euler-Lagrange equation becomes Eq. (23).

$$M_{ii}\ddot{x}_i + \sum_{j=1}^{6}\left[K_h\sum_{k=1}^{3}\mathbf{R}_a(k,i)\mathbf{R}_a(k,j) + K_v\sum_{k=4}^{6}\mathbf{R}_a(k,i)\mathbf{R}_a(k,j)\right]x_j = 0 \tag{23}$$

$$\frac{d}{dt}\left(\frac{\partial L}{\partial \dot{x}_i}\right) = \frac{d}{dt}\left(\frac{\partial T}{\partial \dot{x}_i}\right) = M_{ii}\ddot{x}_i \tag{24}$$

$$where\ M = \begin{bmatrix} m & & & & & \\ & m & & & & \\ & & m & & & \\ & & & I_{xx} & & \\ & & & & I_{yy} & \\ & & & & & I_{zz} \end{bmatrix} \tag{25}$$

Eq. (23) is represented in matrix form,

$$\mathbf{M}\ddot{\mathbf{X}} + \mathbf{K}\mathbf{X} = 0 \tag{26}$$

By applying Laplace transformation to Eq. (26), following equation is obtained.

$$(\mathbf{M}s^2 + \mathbf{K})\mathbf{X} = 0 \tag{27}$$

Moreover, by substituting s with jw and finding w_i, we can obtain natural frequency.

$$\left|-\omega_i^2\mathbf{M} + \mathbf{K}\right| = 0 \tag{28}$$

4.3 Verification of dynamic modes by FEA and experiment

To verify the theoretical analysis of previous Section, we performed the modal analysis with FEA software. First six mode shapes coincide with the fundamental six DOF motions. Corresponding natural frequencies of vibration and mode shapes are depicted in Fig. 10. Arrows shown in modes 3, 5, and 6 imply directions of deformation. Modes 1, 2, and 3 are related to out-of-plane motion whereas modes 4, 5, and 6 are related to in-plane motion.

In addition, by applying the white noise to the precision parallel mechanism, six natural frequencies are obtained as shown in Fig. 11. The experimental transmissibility T_{ij} is obtained using Eq. (29)

$$T_{ij} = \frac{G_{ij}}{G_{ii}} \tag{29}$$

where the first subscript i of the spectral density G_{ij} represents the i-th input signal for actuation and the second subscript j represents the j-th sensor signal. (See Fig. 2. Actuator 1, 2, and 3 are related to in-plane motion and actuator 4, 5, and 6 are related to out-of-plane motion respectively). Note that the relationships between the input from the sensors and the output to the motions of the precision mechanism are included in the previous research.[18]

In Fig. 12, two kinds of analyses (theoretical analysis and FEA simulation) and the experimental result are compared. Although the theoretical analysis and experiments were conducted without damping factor, which can make the natural frequency lower in some measure, the theoretical modal analysis is useful in identifying the effects of design variables in the initial design phase of precision parallel mechanisms and enabling them to respond to specification alteration.

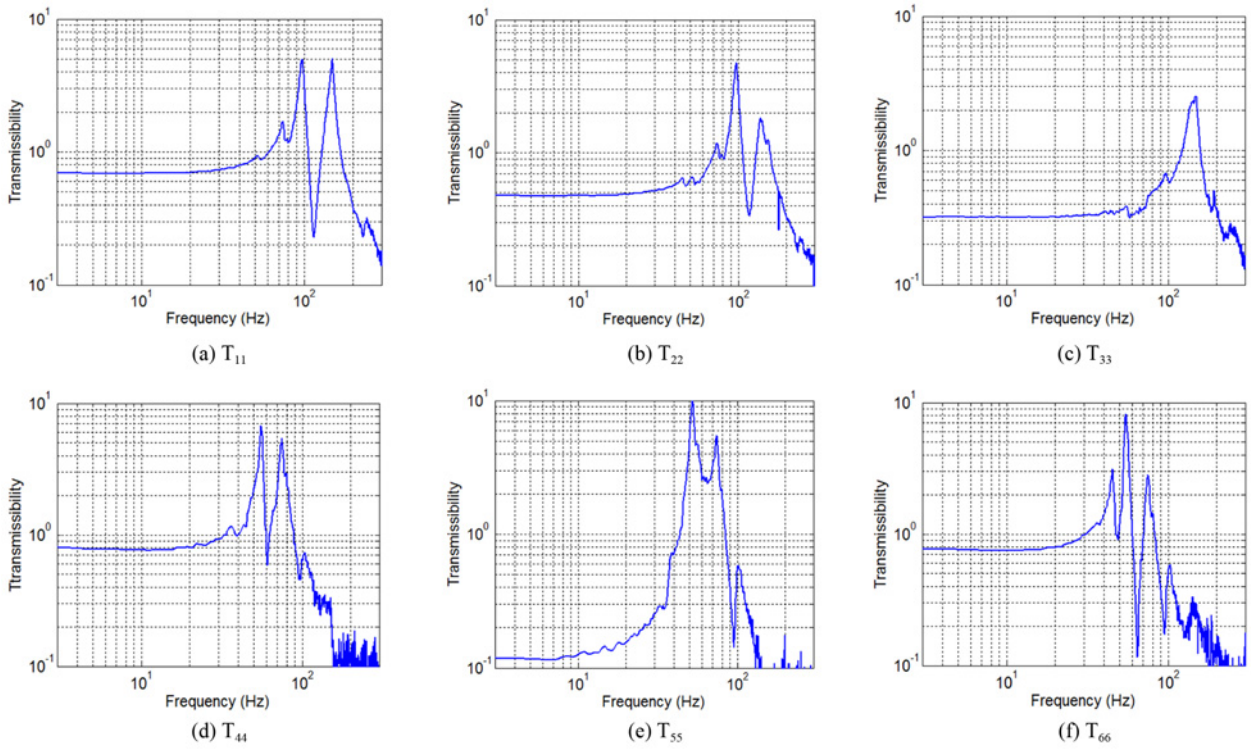

Fig. 11 Experimental results for the six fundamental modes

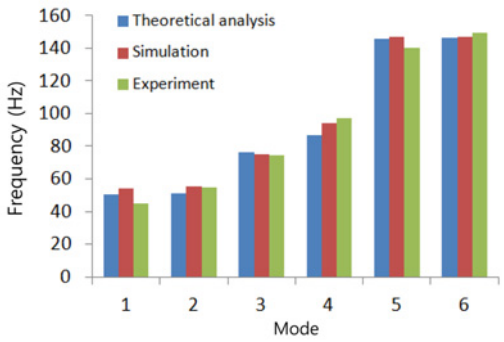

Fig. 12 Comparison of the natural frequencies of vibration for the first six modes: theoretical analysis, FEA, and experimental results

5. Conclusions

A 6-DOF ultra-precision parallel mechanism was designed in order to facilitate new precision processes such as wafer level bonding, nano-imprinting, and micro-bonding. Lost motion is one of the inherent drawbacks of the flexure-based parallel mechanisms. The analytic investigation for the stiffness directionality and lost motions in the horizontal and vertical actuation units, which were tactically designed for the precision positioning, was carried out in this research. The analysis results proved that the lost motion was linearly proportional to commanded displacement and that the stiffness on the horizontal plane was not directional. Experimental dynamic modes of the parallel mechanism coincided with the modes calculated from the linear mapping matrices, which were derived from forward and backward kinematics of the mechanism. Physical meanings of elements of the linear mapping matrices played an important role in mathematical manipulation for modal analysis. The developed methodologies to analyze the lost motion and modal analysis of 6-DOF precision positioner is expected to be useful for succeeding researches on flexure-based precision parallel mechanisms with 6-DOF.

ACKNOWLEDGEMENT

This paper was partly supported by the research program 2016 of Dongyang Mirae University in South Korea.

REFERENCES

1. Yang, R., Jouaneh, M., and Schweizer, R., "Design and Characterization of a Low-Profile Micropositioning Stage," Precision Engineering, Vol. 18, No. 1, pp. 20-29, 1996.
2. Chen, M.-Y., Huang, S.-C., Hung, S.-K., and Fu, L.-C., "Design and Implementation of a New Six-DOF Maglev Positioner with a Fluid Bearing," IEEE/ASME Transactions on Mechatronics, Vol. 16, No. 3, pp. 449-458, 2011.
3. Chang, S. H. and Du, B. C., "A Precision Piezodriven Micropositioner Mechanism with Large Travel Range," Review of Scientific Instruments, Vol. 69, No. 4, pp. 1785-1791, 1998.
4. Yao, Q., Dong, J., and Ferreira, P. M., "Design, Analysis,

Fabrication and Testing of a Parallel-Kinematic Micropositioning XY Stage," International Journal of Machine Tools and Manufacture, Vol. 47, No. 6, pp. 946-961, 2007.

5. Kim, H. S., Cho, Y. M., and Moon, J. H., "Active Vibration Control Using a Novel Three-DOF Precision Micro-Stage," Smart Materials and Structures, Vol. 19, No. 5, Paper No. 055001, 2010.
6. Shin, H., Lee, S., Jeong, J. I., and Kim, J., "Antagonistic Stiffness Optimization of Redundantly Actuated Parallel Manipulators in a Predefined Workspace," IEEE/ASME Transactions on Mechatronics, Vol. 18, No. 3, pp. 1161-1169, 2013.
7. Gao, P. and Swei, S.-M., "A Six-Degree-of-Freedom Micro-Manipulator Based on Piezoelectric Translators," Nanotechnology, Vol. 10, No. 4, pp. 447-452, 1999.
8. Choi, K.-B. and Lee, J. J., "Passive Compliant Wafer Stage for Single-Step Nano-Imprint Lithography," Review of Scientific Instruments, Vol. 76, No. 7, Paper No. 075106, 2005.
9. Moon, J.-H., Pahk, H. J., and Lee, B.-G., "Design, Modeling, and Testing of a Novel 6-DOF Micropositioning Stage with Low Profile and Low Parasitic Motion," The International Journal of Advanced Manufacturing Technology, Vol. 55, Nos. 1-4, pp. 163-176, 2011.
10. Fleming, A. J., Berriman, G., and Yong, Y. K., "Design, Modeling, and Characterization of an XY Nanopositioning Stage Constructed from a Single Sheet of Piezoelectric Material," Proc. of IEEE International Conference on Advanced Intelligent Mechatronics (AIM), pp. 1333-1338, 2016.
11. Huang, S.-C. and Dao, T.-P., "Design and Computational Optimization of a Flexure-based XY Positioning Platform Using FEA-based Response Surface Methodology," International Journal of Precision Engineering and Manufacturing, Vol. 17, No. 8, pp. 1035-1048, 2016.
12. Hu, K., Kim, J. H., Schmiedeler, J., and Menq, C.-H., "Design, Implementation, and Control of a Six-Axis Compliant Stage," Review of Scientific Instruments, Vol. 79, No. 2, Paper No. 025105, 2008.
13. Choi, S. B., Han, S. S., and Lee, Y. S., "Fine Motion Control of a Moving Stage Using a Piezoactuator Associated with a Displacement Amplifier," Smart Materials and Structures, Vol. 14, No. 1, pp. 222-230, 2004.
14. Yue, Y., Gao, F., Zhao, X., and Ge, Q. J., "Relationship Among Input-Force, Payload, Stiffness and Displacement of a 3-DOF Perpendicular Parallel Micro-Manipulator," Mechanism and Machine Theory, Vol. 45, No. 5, pp. 756-771, 2010.
15. Awtar, S. and Sen, S., "A Generalized Constraint Model for Two-Dimensional Beam Flexures: Nonlinear Load-Displacement Formulation," Journal of Mechanical Design, Vol. 132, No. 8, Paper No. 081008, 2010.
16. Su, H.-J., Shi, H., and Yu, J., "A Symbolic Formulation for Analytical Compliance Analysis and Synthesis of Flexure Mechanisms," Journal of Mechanical Design, Vol. 134, No. 5, Paper No. 051009, 2012.
17. Lu, S.-S. and Yan, P., "A Stiffness Modeling Approach for Multi-Leaf Spring Mechanism Supporting Coupling Error Analysis of Nano-Stages," International Journal of Precision Engineering and Manufacturing, Vol. 18, No. 6, pp. 863-870, 2017.
18. Shin, H. and Moon, J.-H., "Design of a Double Triangular Parallel Mechanism for Precision Positioning and Large Force Generation," IEEE/ASME Transactions on Mechatronics, Vol. 19, No. 3, pp. 862-871, 2014.